SiLENSe™

Physics Summary

Version 6.4 & Version 6.4 Laser Edition

STR IP Holding, LLC, Richmond, VA, USA

Customer Support: SimuLED-support@str-soft.com

Software Sales: STR-sales@str-soft.com

Contents

1 Introduction

One-dimensional SiLENSe package is intended for simulation of heterostructures used in light-emitting diodes (LEDs) and laser diodes (LDs). The software simulates band diagram as a function of the p-n junction bias, distribution of electron and hole concentrations, electron and hole current density, radiative and non-radiative recombination rates, carrier energy levels and wave functions in the quantum wells, emission and gain spectra, internal quantum efficiency (IQE), injection efficiency, etc.

Built-in database of material properties includes both zinc-blende (cubic) and wurtzite materials, such as AlInGaN, AlGaInAs, AlGaInP, and others. Specific features of III-nitride materials like strong piezoeffect, spontaneous electric polarization, low efficiency of acceptor activation, and high threading dislocation density inherent in III-nitride epitaxial layers are included into the model.

The software enables the analysis of graded-index heterostructures, which is important for development of novel semiconductor devices by using the bandgap engineering principles.

Laser Edition of the package also enables computation of the waveguide modes and prediction of the threshold characteristics.

The software implements one-dimensional drift-diffusion model. This document describes the basic physical models implemented in the SiLENSe package.

2 Strain, Piezoeffect, and Spontaneous Polarization

An LED heterostructure is considered as a stack of epitaxial layers pseudo-morphically grown on an underlying template/substrate layer. For structures which are not lattice-matched to the substrate, such as GaN/sapphire, a buffer layer serves as the template due to strain relaxation at the buffer/substrate interface. By default, other epilayers are assumed to have the lateral lattice constant equal to that of the template layer. Optionally, user can directly specify the lateral lattice constant $a_{strained}$ of some layer or specify a degree of relaxation, ξ, in a layer (these two options can not be used simultaneously). If relaxation degree is specified, the strained lattice constant in the layer is calculated as

$$a_{strained} = \xi a_{free} + (1 - \xi)\, a^0_{strained} \tag{2.1}$$

where a_{free} is the free-standing lattice constant for the layer of specified composition and $a^0_{strained}$ is the strained lattice constant at the top of the underlying (previous) layer. The first layer is assumed to have no strain, i.e. $a_{strained} = a_{free}$, until opposite is not specified explicitly by setting the value of the strained lattice constant. Eventually, the evolution of the strained lattice constant $a_{strained}$ is calculated for the whole structure starting from the first layer and going up layer by layer. In vast majority of practical cases, the degree of relaxation is zero for all the layers and so the strained lattice constant equals to that of the first layer. Use of degree of relaxation or direct specification of the strained lattice constant are used rarely.

Let us define the coordinate system related to the epilayers (x', y', z') in such a way that axis z' is directed normal to the epilayers. Let the coordinate system related to the crystollagraphic axis (x, y, z) be rotated compared to epilayers around x axis, so that $x = x'$. Below, we will denote with $'$ symbol the values defined in the coordinate system related to the epilayers. Note that all material parameters, such as stiffness constants

C_{ij} and piezoelectric constants e_{ij}, are defined in the Voigt notation [1] in the coordinate system related to the crystallographic axis. In analysis of the strain effect on the band structure in Sections (3) and (4) we also use strain components in the coordinates related to the crystal lattice.

NB Outside this section and Sections (3) and (4), we will denote by z the direction normal to the epilayers.

NB In literature, there are two definitions for the components of the strain tensor, u and ε, which are same for normal strain and differs by the factor of 2 for shear strain

$$\begin{array}{cccccccc} u_{xx} & = & \varepsilon_{xx} & u_{yy} & = & \varepsilon_{yy} & u_{zz} & = & \varepsilon_{zz} \\ u_{xy} & = & \frac{1}{2}\varepsilon_{xy} & u_{yz} & = & \frac{1}{2}\varepsilon_{yz} & u_{xz} & = & \frac{1}{2}\varepsilon_{xz} \end{array} \quad . \tag{2.2}$$

NB Starting from version 6.3, output for strain components presents strain components u_{ij} in the coordinate system related to the crystallographic axes. In older versions, strain components ε was outputted (the difference is only in the shear strain component).

2.1 Zinc-Blende Materials

For zinc-blende crystals, we will consider only three most popular growth directions: [001], [011], and [111]. Below, components of the strain tensor are expressed in terms of stiffness constants C_{ij} and lattice mismatch parameter η

$$\eta = \frac{a_{free} - a_{strained}}{a_{free}} \quad . \tag{2.3}$$

Orientation [001]

$$u_{xx} = u_{yy} = -\eta \quad , \quad u_{zz} = 2\,\eta\, C_{12}/C_{11} \quad , \quad u_{xy} = u_{yz} = u_{xz} = 0 \tag{2.4}$$

Orientation [011]

$$\begin{aligned} u_{xx} = -\eta \quad , \quad u_{yy} = u_{zz} = \eta\, \frac{C_{12} - 2\,C_{44}}{C_{11} + C_{12} + 4\,C_{44}} \\ u_{xy} = u_{xz} = 0 \quad , \quad u_{yz} = \eta\, \frac{C_{11} + 2\,C_{12}}{C_{11} + C_{12} + 4\,C_{44}} \end{aligned} \tag{2.5}$$

Orientation [111]

$$\begin{aligned} u_{xx} = u_{yy} = u_{zz} = -\,\eta\, \frac{4\,C_{44}}{C_{11} + 2\,C_{12} + 4\,C_{44}} \\ u_{xy} = u_{yz} = u_{xz} = \eta\, \frac{C_{11} + 2\,C_{12}}{C_{11} + 2\,C_{12} + 4\,C_{44}} \end{aligned} \tag{2.6}$$

For this orientation, there is a non-zero component of piezoelectric polarization directed normal to the epilayers

$$P_z = 2\sqrt{3}\, e_{14}\, \eta\, \frac{C_{11} + 2\,C_{12}}{C_{11} + 2\,C_{12} + 4\,C_{44}} \quad . \tag{2.7}$$

2.2 Wurtzite Materials

Generally, strain and piezoeffect in polar, nonpolar, and semipolar heterostructures are described within the approach suggested in [2], while the derivation of the final equations is different, and the misprints in the paper are also fixed.

For wurtzite crystals, two lattice mismatches η_a and η_c are introduced regarding lattice constants a and c, respectively, in a way similar to (2.3)

$$\eta_a = \frac{a_{free} - a_{strained}}{a_{free}} \quad , \quad \eta_c = \frac{c_{free} - c_{strained}}{c_{free}} \quad . \tag{2.8}$$

Semi-polar orientations For the general case of a semi-polar structure, let us define the inclination angle θ as the angle between the normal to the epilayers (axis z') and the hexagonal crystal axis z. Then lattice mismatch along $x = x'$ axis equals to η_a, while lattice mismatch along the axis y' depends on the inclination

$$\eta_y = \eta_a \cos^2\theta + \eta_c \sin^2\theta \tag{2.9}$$

In the coordinate system related to the crystallographic axes, the components of the compliance matrix S_{ij} are related to the stiffness constants C_{ij} as

$$\begin{aligned}
S_{11} &= \frac{C_{11}C_{33} - C_{13}^2}{(C_{11} - C_{12})\left(C_{33}(C_{11} + C_{12}) - 2C_{13}^2\right)} \quad , \quad S_{33} = \frac{C_{11} + C_{12}}{C_{33}(C_{11} + C_{12}) - 2C_{13}^2} \\
S_{13} &= \frac{C_{13}^2 - C_{33}C_{12}}{(C_{11} - C_{12})\left(C_{33}(C_{11} + C_{12}) - 2C_{13}^2\right)} \quad , \quad S_{13} = \frac{-C_{13}}{C_{33}(C_{11} + C_{12}) - 2C_{13}^2} \\
S_{44} &= 1/C_{44} \quad , \quad S_{66} = 2(S_{11} - S_{12})
\end{aligned} \tag{2.10}$$

In the coordinate system related to the epitaxial layers, there are only two non-zero components of the stress tensor

$$\sigma_{x'x'} = -\frac{\eta_a S_{22}^* - \eta_y S_{12}^*}{S_{11}S_{22}^* - (S_{12}^*)^2} \quad , \quad \sigma_{y'y'} = -\frac{\eta_y S_{11} - \eta_a S_{12}^*}{S_{11}S_{22}^* - (S_{12}^*)^2} \tag{2.11}$$

where coefficients S^* depend on the inclination angle θ

$$\begin{aligned}
S_{12}^* &= S_{12}\cos^2\theta + S_{13}\sin^2\theta \qquad (2.12) \\
S_{22}^* &= S_{12}\cos^2\theta + S_{13}\sin^2\theta + \frac{1}{4}(2S_{13} + S_{44} - S_{11} - S_{33})\sin^2 2\theta
\end{aligned}$$

In the coordinate system related to the crystallographic axes, the strain tensor has 4 non-zero components (note that $\sigma_{xx} = \sigma_{x'x'}$ and $\varepsilon_{yz} = 2u_{yz}$)

$$\begin{aligned}
u_{xx} &= -\eta_a \\
u_{yy} &= S_{12}\,\sigma_{x'x'} + \left(S_{11}\cos^2\theta + S_{13}\sin^2\theta\right)\sigma_{y'y'} \\
u_{zz} &= S_{13}\,\sigma_{x'x'} + \left(S_{13}\cos^2\theta + S_{33}\sin^2\theta\right)\sigma_{y'y'} \qquad (2.13) \\
u_{yz} &= -\frac{1}{4}S_{44}\,\sigma_{y'y'}\sin 2\theta \qquad (2.14)
\end{aligned}$$

The total polarization in the direction normal to epilayers is a sum of spontaneous polarization and piezoelectric polarization

$$P_{z'}^{tot} = P_z^{spont}\cos\theta + d_{31}^{'}\sigma_{x'x'} + d_{32}^{'}\sigma_{y'y'} \tag{2.15}$$

where P^{spont} is the spontaneous polarization of wurtzite crystal which has only z-component because of symmetry, and $d_{ij}^{'}$ are calculated from the piezoelectric constants e_{ij} and compliance matrix S as following

$$d_{31}^{'} = d_{31}\cos\theta \quad , \quad d_{32}^{'} = \left(d_{31}\cos^2\theta + d_{33}\sin^2\theta - d_{15}\sin^2\theta\right)\cos\theta \tag{2.16}$$

$$d_{31} = e_{31}\left(S_{11}+S_{12}\right) + e_{33}S_{13} \quad , \quad d_{33} = 2e_{31}S_{13} + e_{33}S_{33} \quad , \quad d_{15} = e_{15}S_{44} \tag{2.17}$$

The dielectric constant of wurtzite crystals is anisotropic with components k_z for the direction along the [0001] direction and k_t along the plane normal to this direction. Piezoeffect also causes anisotropic contribution into the dielectric constant. Finally, the effective dielectric constant in the direction normal to the epilayers can be expressed as

$$k^* = \left(k_z - \frac{2e_{31}^2\left(S_{11}+S_{12}\right) + 4e_{31}e_{33}S_{13} + e_{33}^2S_{33}}{k_0}\right)\cos^2\theta + \left(k_t - \frac{e_{15}^2S_{44}}{k_0}\right)\sin^2\theta \tag{2.18}$$

where k_0 is the dielectric permittivity of vacuum.

Polar orientations [0001] and [000-1] For polar orientation the above equations are simplified considerably, providing the strain components as

$$\begin{aligned} \varepsilon_{xx} = \varepsilon_{yy} &= -\eta \\ \varepsilon_{zz} &= 2\,\eta\,\frac{C_{13}}{C_{33}} \\ \varepsilon_{xy} = \varepsilon_{xz} = \varepsilon_{yz} &= 0 \end{aligned} \tag{2.19}$$

and total polarization in the direction normal to epilayers reads as

$$P_{z'}^{tot} = \pm\left(P_z^{spont} + e_{31}\left(\varepsilon_{xx}+\varepsilon_{yy}\right) + e_{33}\varepsilon_{zz}\right) = \pm\left(P^{spont} - 2\eta\left(e_{31} - e_{33}\frac{C_{13}}{C_{33}}\right)\right) \tag{2.20}$$

where sign is "+" for [0001] orientation and "−" for [000-1] orientation. Note that above expressions does not include the lattice mismatch η_c.

3 Band Structure (Zinc-Blende Materials)

The energy gap in a semiconductor layer of some composition is calculated as following. First, the energy gap is calculated without strain as discussed in Sec. (3.1). The energy gap without strain effect is used to calculate other material parameters depending on the energy gap, such as effective masses, refractive index, and so on. Second, the strain effect on the band structure are added as discussed in Secs. (3.2-3.3). The deformation potentials used in these calculations are calculated for a certain alloy composition by linear interpolation of their values for binary compounds.

3.1 Band structure without strain

Without strain, the position of valence band subbands is determined by the ionization energy Υ and spin-orbital splitting Δ:

$$E_{hh} = E_{lh} = -\Upsilon, \qquad E_{sh} = -\Upsilon - \Delta \qquad . \tag{3.1}$$

Energies of three valleys of the conduction band are calculated from the energy gap:

$$E_C^\nu = -\Upsilon + E_G^\nu \quad (\text{where } \nu = \Gamma, X, L) \tag{3.2}$$

Temperature dependence of the energy gap of binary compounds is described by Varshni parameters:

$$E_G^\nu(T) = E_G^\nu(0K) - \frac{\alpha^\nu T^2}{T + \beta^\nu} \quad . \tag{3.3}$$

For alloys, we first calculate the energy gap of the respective binary compounds with account of temperature. Next, we calculate the energy gap of the alloy by linear interpolation of the energy gap of binary compounds and add second order term describing bowing of the energy gap. For quaternary alloys, there are two different interpolations are used depending on the alloy type.

Alloys where atoms are varied only in one sublattice ($A_xB_yC_{1-x-y}D$):

$$\begin{aligned} E_G^{ABCD} &= xE_G^{AD} + yE_G^{BD} + (1-x-y)E_G^{CD} \\ &-xyb^{ABD} - x(1-x-y)b^{ACD} - y(1-x-y)b^{BCD} \end{aligned} \tag{3.4}$$

where b^{ABD}, b^{ACD}, and b^{BCD} are bowing parameters of the respective ternary compounds.

Alloys where atoms are varied in both sublattices ($A_xB_{1-x}C_yD_{1-y}$):

$$\begin{aligned} E_G^{ABCD} &= xyE_G^{AC} + (1-x)yE_G^{BC} + x(1-y)E_G^{AD} + (1-x)(1-y)E_G^{BD} \\ &-xy(1-x)b^{ABC} - x(1-x)(1-y)b^{ABD} - xy(1-y)b^{ACD} - (1-x)y(1-y)b^{BCD} \end{aligned} \tag{3.5}$$

where b^{ABC}, b^{ABD}, b^{ACD}, and b^{BCD} are bowing parameters of the respective ternary compounds.

3.2 Strain effect on conduction band

With account of strain, conduction band edge in Γ-valley is given by

$$E_C^\Gamma = -\Upsilon + E_G^\Gamma + \pi^\Gamma \quad , \quad \pi^\Gamma = a_c(u_{xx} + u_{yy} + u_{zz}) \tag{3.6}$$

where a_c is the conduction band deformation potential and u_{ij} are components of the strain tensor in the coordinate system related to the crystal lattice. Generally, strain leads to splitting of X and L valleys into 3 and 4 subbands, respectively

$$E_C^{X,L} = -\Upsilon + E_G^{X,L} + \pi_{ijk}^{X,L} \tag{3.7}$$

where ijk denotes the direction to the particular minimum of the X or L valley.

X-valley:

$$\begin{aligned} \pi_{100}^X &= \Xi_d^X(u_{xx} + u_{yy} + u_{zz}) + \Xi_u^X u_{xx} \\ \pi_{010}^X &= \Xi_d^X(u_{xx} + u_{yy} + u_{zz}) + \Xi_u^X u_{yy} \\ \pi_{001}^X &= \Xi_d^X(u_{xx} + u_{yy} + u_{zz}) + \Xi_u^X u_{zz} \end{aligned} \tag{3.8}$$

L-valley:

$$\begin{aligned}
\pi^L_{111} &= \left(\Xi^L_d + \tfrac{1}{3}\,\Xi^L_u\right)(u_{xx}+u_{yy}+u_{zz}) + \tfrac{2}{3}\,\Xi^L_u\,(u_{yz}+u_{xz}+u_{xy}) \\
\pi^L_{-111} &= \left(\Xi^L_d + \tfrac{1}{3}\,\Xi^L_u\right)(u_{xx}+u_{yy}+u_{zz}) + \tfrac{2}{3}\,\Xi^L_u\,(u_{yz}-u_{xz}-u_{xy}) \\
\pi^L_{-1-11} &= \left(\Xi^L_d + \tfrac{1}{3}\,\Xi^L_u\right)(u_{xx}+u_{yy}+u_{zz}) + \tfrac{2}{3}\,\Xi^L_u\,(-u_{yz}-u_{xz}+u_{xy}) \\
\pi^L_{1-11} &= \left(\Xi^L_d + \tfrac{1}{3}\,\Xi^L_u\right)(u_{xx}+u_{yy}+u_{zz}) + \tfrac{2}{3}\,\Xi^L_u\,(-u_{yz}+u_{xz}-u_{xy})
\end{aligned} \tag{3.9}$$

Let us substitute strain components for typical growth directions listed in Sec. (2.1) into equations (3.8-3.9). Eventually, there are only 3 or 4 band edges for both X and L valleys. Below, we will list final solutions for each growth direction.

[001] (2 energies for X-valley and 1 energy for L-valley):

$$\begin{aligned}
\pi^X_{100} = \pi^X_{010} &= -2\,\Xi^X_d\,\eta\,(1 - C_{12}/C_{11}) - \Xi^X_u\,\eta \\
\pi^X_{001} &= -2\,\Xi^X_d\,\eta\,(1 - C_{12}/C_{11}) + 2\,(C_{12}/C_{11})\,\Xi^X_u\,\eta \\
\pi^L_{111} = \pi^L_{-111} = \pi^L_{-1-11} = \pi^L_{1-11} &= -2\left(\Xi^L_d + \tfrac{1}{3}\,\Xi^L_u\right)\eta\,(1 - C_{12}/C_{11})
\end{aligned} \tag{3.10}$$

[011] (2 energies for both X and L valleys):

$$\begin{aligned}
\pi^X_{100} = &= -\Xi^X_d\;\eta\,\frac{-C_{11}+C_{12}+6C_{44}}{C_{11}+C_{12}+2C_{44}} - \Xi^X_u\;\eta \\
\pi^X_{010} = \pi^X_{001} &= -\Xi^X_d\;\eta\,\frac{-C_{11}+C_{12}+6C_{44}}{C_{11}+C_{12}+2C_{44}} + \Xi^X_u\;\eta\,\frac{C_{11}-2C_{44}}{C_{11}+C_{12}+2C_{44}} \\
\pi^L_{111} = \pi^L_{-111} &= -\left(\Xi^L_d + \tfrac{1}{3}\,\Xi^L_u\right)\;\eta\,\frac{-C_{11}+C_{12}+6C_{44}}{C_{11}+C_{12}+2C_{44}} + \tfrac{2}{3}\,\Xi^L_u\;\eta\,\frac{C_{11}+2C_{12}}{C_{11}+C_{12}+2C_{44}} \\
\pi^L_{-1-11} = \pi^L_{1-11} &= -\left(\Xi^L_d + \tfrac{1}{3}\,\Xi^L_u\right)\;\eta\,\frac{-C_{11}+C_{12}+6C_{44}}{C_{11}+C_{12}+2C_{44}} - \tfrac{2}{3}\,\Xi^L_u\;\eta\,\frac{C_{11}+2C_{12}}{C_{11}+C_{12}+2C_{44}}
\end{aligned} \tag{3.11}$$

[111] (1 energy for X-valley and 2 energies for L-valley):

$$\begin{aligned}
\pi^X_{100} = \pi^X_{010} = \pi^X_{001} &= -\left(\Xi^X_d + \tfrac{1}{3}\,\Xi^X_u\right)\;\eta\,\frac{12C_{44}}{C_{11}+2C_{12}+4C_{44}} \\
\pi^L_{111} &= -\Xi^L_d\;\eta\,\frac{12C_{44}}{C_{11}+2C_{12}+4C_{44}} + 2\,\Xi^L_u\;\eta\,\frac{C_{11}+2C_{12}-2C_{44}}{C_{11}+2C_{12}+4C_{44}} \\
\pi^L_{-111} = \pi^L_{-1-11} = \pi^L_{1-11} &= -\Xi^L_d\;\eta\,\frac{12C_{44}}{C_{11}+2C_{12}+4C_{44}} + \tfrac{2}{3}\,\Xi^L_u\;\eta\,\frac{C_{11}+2C_{12}+6C_{44}}{C_{11}+2C_{12}+4C_{44}}
\end{aligned} \tag{3.12}$$

NB: Please do not confuse the growth direction, which determines the relations between the components of the strain tensor, and direction related to the particular minimum of X or L valley (subscript in $\pi^{X,L}_{ijk}$). They are denoted in the same way, but the meaning is very different!

3.3 Strain effect on valence band

Below a_v, b_v, and d_v are three conduction band deformation potentials, and

$$P_\varepsilon = -a_v\,(u_{xx}+u_{yy}+u_{zz})$$

(below we will give it in explicit form in terms of lattice mismatch and stiffness constants). For growth directions [001] and [111], the valence band subbands can be expressed in a compact form.

[001]:

$$\begin{aligned} E_{hh} &= -\Upsilon - P_\varepsilon - Q_\varepsilon \\ E_{lh} &= -\Upsilon - P_\varepsilon + \frac{1}{2}\left(Q_\varepsilon - \Delta + \sqrt{(Q_\varepsilon + \Delta)^2 + 8Q_\varepsilon^2}\right) \\ E_{sh} &= -\Upsilon - P_\varepsilon + \frac{1}{2}\left(Q_\varepsilon - \Delta - \sqrt{(Q_\varepsilon + \Delta)^2 + 8Q_\varepsilon^2}\right) \end{aligned} \tag{3.13}$$

where

$$P_\varepsilon = 2\,a_v\,\eta\,\left(1 - C_{12}/C_{11}\right) \quad , \quad Q_\varepsilon = b_v\,\eta\,\left(1 + 2C_{12}/C_{11}\right) \quad . \tag{3.14}$$

[111]:

$$\begin{aligned} E_{hh} &= -\Upsilon - P_\varepsilon - R_\varepsilon \\ E_{lh} &= -\Upsilon - P_\varepsilon + \frac{1}{2}\left(R_\varepsilon - \Delta + \sqrt{(R_\varepsilon + \Delta)^2 + 8R_\varepsilon^2}\right) \\ E_{sh} &= -\Upsilon - P_\varepsilon + \frac{1}{2}\left(R_\varepsilon - \Delta - \sqrt{(R_\varepsilon + \Delta)^2 + 8R_\varepsilon^2}\right) \end{aligned} \tag{3.15}$$

where

$$P_\varepsilon = a_v\,\eta\,\frac{12\,C_{44}}{C_{11} + 2C_{12} + 4C_{44}} \quad , \quad R_\varepsilon = \sqrt{3}\,d_v\,\eta\,\frac{C_{11} + 2C_{12}}{C_{11} + 2C_{12} + 4C_{44}} \quad . \tag{3.16}$$

[011]: Valence band subbands are roots of a third-order equation, and final expressions are quite complicated.

3.4 Effective masses

Electron effective mass in Γ valley is calculated as following

$$\frac{m_0}{m^\Gamma} = 1 + 2F + E^P\,\frac{\left(E_G^\Gamma + \frac{2}{3}\Delta\right)}{E_G^\Gamma\,\left(E_G^\Gamma + \Delta\right)} \tag{3.17}$$

where E_P is Kane's matrix element and parameter F corresponds to contribution of the remote bands.

This equation is used by default, i.e. if "Parameterization" type is specified for this property. Alternatively, user can directly specify the the value of this property by choosing "Constant" or "Function" type for pure materials and "Bowing" or "Function" type for alloys.

Electron effective masses in X and L valleys are specified in dataset of material properties. For alloys, inverse effective masses of the respective binary compounds are interpolated linearly. Different interpolations are used for two types of quaternary alloys.

$A_xB_yC_{1-x-y}D$ alloys:

$$m_{l,t}^{X,L} = \left(\frac{x}{m_{l,t}^{X,L}(AD)} + \frac{y}{m_{l,t}^{X,L}(BD)} + \frac{1-x-y}{m_{l,t}^{X,L}(CD)} \right)^{-1} \quad . \tag{3.18}$$

$A_xB_{1-x}C_yD_{1-y}$ alloys:

$$m_{l,t}^{X,L} = \left(\frac{xy}{m_{l,t}^{X,L}(AC)} + \frac{(1-x)y}{m_{l,t}^{X,L}(BC)} + \frac{x(1-y)}{m_{l,t}^{X,L}(AD)} + \frac{(1-x)(1-y)}{m_{l,t}^{X,L}(BD)} \right)^{-1} \quad . \tag{3.19}$$

This interpolation is used by default, i.e. if "Parameterization" type is specified for this property in alloys. Alternatively, user can specify another rule for interpolation of this property by choosing "Bowing" or "Function" type.

Hole effective masses are assumed to be isotropic and calculated from Luttinger parameters as following

$$\frac{m_0}{m^{hh}} = \gamma_1 - 2\gamma \qquad \frac{m_0}{m^{lh}} = \gamma_1 + 2\gamma \qquad \frac{m_0}{m^{sh}} = \gamma_1 \qquad \gamma = (2\gamma_2 + 3\gamma_3)/5 \quad . \tag{3.20}$$

This equation is used by default, i.e. if "Parameterization" type is specified for this property. Alternatively, user can directly specify the the value of this property by choosing "Constant" or "Function" type for pure materials and "Bowing" or "Function" type for alloys.

Luttinger parameters are specified at 300 K and their temperature dependence is assumed to be inversely proportional to the energy gap

$$\gamma_k(T) = \gamma_k(300K)\, E_G^{\Gamma}(300K) / E_G^{\Gamma}(T) \quad . \tag{3.21}$$

Keeping the same assumption for alloys, we obtain the following equation for interpolating Luttinger parameters. Different interpolations are used for two types of quaternary alloys.

For $A_xB_yC_{1-x-y}D$ alloys:

$$\gamma_k E_G^{\Gamma} = x\gamma_k(AD)\, E_G^{\Gamma}(AD) + y\gamma_k(BD)\, E_G^{\Gamma}(BD) + (1-x-y)\,\gamma_k(CD)\, E_G^{\Gamma}(CD) \quad . \tag{3.22}$$

For $A_xB_{1-x}C_yD_{1-y}$ alloys:

$$\begin{aligned} \gamma_k E_G^{\Gamma} = {} & xy\gamma_k(AC)\, E_G^{\Gamma}(AC) + (1-x)y\gamma_k(BC)\, E_G^{\Gamma}(BC) + \\ & x(1-y)\gamma_k(AD)\, E_G^{\Gamma}(AD) + (1-x)(1-y)\gamma_k(BD)\, E_G^{\Gamma}(BD) \quad . \end{aligned} \tag{3.23}$$

4 Band Structure (Wurtzite Materials)

4.1 Band structure of binary compounds

All III-nitride wurtzite materials (AlN, GaN, and InN) are direct gap materials with X and L valleys being far above the Γ valley, so we will neglect X and L valleys and omit index Γ for the energy gap, electron effective masses, etc. The conduction band edge is given by

$$E_C = -\Upsilon + E_G + \pi \qquad , \qquad \pi = a_c^t \left(u_{xx} + u_{yy}\right) + a_c^z \, u_{zz} \tag{4.1}$$

where temperature dependence of the energy gap E_G is given by Varshni parameters similarly to Eq. (3.3), a_c^t and a_c^z are the conduction band deformation potentials with respect to lateral and vertical directions, and u_{ij} are components of the strain tensor in the coordinate system related to the crystal lattice.
The energy bands of heavy (hh), light (lh), and split-off (sh) holes are calculated as

$$\begin{aligned} E_{hh} &= -\Upsilon + L_\varepsilon + T_\varepsilon \\ E_{lh} &= -\Upsilon + L_\varepsilon - \frac{\Delta_1 + 3\Delta_2 - T_\varepsilon}{2} + \sqrt{\left(\frac{\Delta_1 - \Delta_2 + T_\varepsilon}{2}\right)^2 + 2\Delta_3^2} \\ E_{sh} &= -\Upsilon + L_\varepsilon - \frac{\Delta_1 + 3\Delta_2 - T_\varepsilon}{2} - \sqrt{\left(\frac{\Delta_1 - \Delta_2 + T_\varepsilon}{2}\right)^2 + 2\Delta_3^2} \end{aligned} \tag{4.2}$$

4.2 Effective masses

Carrier effective masses in wurtzite materials are anisotropic. Below, indices z and t denote the direction along the crystal [0001] axis and the plane normal to this direction, respectively.

Electron effective masses are calculated as following

$$\begin{aligned} \frac{m_0}{m_z^e} &= 1 + 2F_z + E_z^P \frac{E_G + 2\Delta_2}{\left(E_G + \Delta_1 + \Delta_2\right)\left(E_G + 2\Delta_2\right) - 2\Delta_3^2} \\ \frac{m_0}{m_t^e} &= 1 + 2F_t + E_t^P \frac{\left(E_G + \Delta_1 + \Delta_2\right)\left(E_G + \Delta_2\right) - \Delta_3^2}{E_G\left[\left(E_G + \Delta_1 + \Delta_2\right)\left(E_G + 2\Delta_2\right) - 2\Delta_3^2\right]} \end{aligned} \tag{4.3}$$

where $E_{z,t}^P$ are Kane's matrix elements and parameters $F_{z,t}$ correspond to contribution of the remote bands.

This equation is used by default, i.e. if "Parameterization" type is specified for this property. Alternatively, user can directly specify the the value of this property by choosing "Constant" or "Function" type for pure materials and "Bowing" or "Function" type for alloys.

Hole effective masses are calculated from Luttinger parameters A_i as following

$$\begin{aligned} \frac{m_0}{m_z^{hh}} &= -\left(A_1 + A_3\right) & \frac{m_0}{m_z^{lh}} &= -\left(A_1 + A_3\right) & \frac{m_0}{m_z^{sh}} &= -A_1 \\ \frac{m_0}{m_t^{hh}} &= -\left(A_2 + A_4 - A_5\right) & \frac{m_0}{m_t^{lh}} &= -\left(A_2 + A_4 + A_5\right) & \frac{m_0}{m_t^{sh}} &= -A_2 \end{aligned} \tag{4.4}$$

This equation is used by default, i.e. if "Parameterization" type is specified for this property. Alternatively, user can directly specify the the value of this property by choosing "Constant" or "Function" type for pure materials and "Bowing" or "Function" type for alloys.

Contrary to zinc blende materials, Luttinger parameters of III-nitrides are assumed to be temperature-independent and linear interpolation is used to calculate their values for alloys.

5 Refractive Index

Approximation for the real part of dielectric constants of zinc-blende semiconductors near the absorption edge has been suggested by Pikhtin and Yas'kov (see review [8] and references therein). Here, a modified model is used, accounting for spectral broadening of the absorption edge. The real part of the dielectric constant ε as a function of photon energy E is approximated by the expression

$$\varepsilon(E) = 1 + \frac{A}{2\pi}\left\{\ln\left(\frac{\left(E_1^2 - E^2\right)^2}{\left(E_g^2 - E^2\right)^2 + E^2\Gamma^2}\right)\right\} + \sum_{k=1}^{2}\frac{G_k}{E_k^2 - E^2} \tag{5.1}$$

where E_g is the lowest energy gap among Γ, X, and L valleys and $E_{1,2}$ are the energies corresponding to major peaks in the imaginary part of dielectric constant. The broadening parameter Γ is introduced empirically [9] in order to exclude divergence in ε at the photon energy equal to the energy gap E_g.

For III-nitride materials, the above approach is modified as following. First, the absorption edge parameter is introduced explicitly and used in Eq. (5.1) instead of the energy gap E_g. Second, the term with $k = 2$ is not used. Third, parameters for ordinary (o) and extraordinary (e) waves are specified as independent parameters (while most of them are the same for both waves).

Refractive index is calculated as $n = \sqrt{\varepsilon}$ and used mainly for computation of the waveguide modes. Also, it is used in calculation of the radiative recombination constant B and free-carrier absorption (Eqs. (7.3) and (11.12), respectively).

Old model Another parameterization of the dielectric constant was used in version 5.15 and all versions released before it

$$\varepsilon(E) = \varepsilon_\infty + A_0\frac{\Gamma_0^2 E\left(2E_0 - E\right)}{\left(E_0^2 + \Gamma_0^2\right)\left[\left(E - E_0\right)^2 + \Gamma_0^2\right]} + A_1\frac{E_1^2\left(E_1^2 - E^2\right)}{\left(E_1^2 - E^2\right)^2 + \left(E\Gamma_1\right)^2} \tag{5.2}$$

Here, E_0 is the absorption edge energy nearly equal to the energy gap and E_1 is the energy of the absorption peak related to higher electron bands. A_0 and A_1 are the dimensionless oscillator strengths of these absorption peaks, Γ_0 and Γ_1 are the broadening parameters, and ε_∞ is the high-frequency dielectric function. For alloys, these values were interpolated linearly, and bowing similar to that for the energy gap was used for E_0.

In the default dataset of version 6.3, the refractive index of three materials (sapphire, SiC-4H, and SiC-6H) is specified by a script function implementing Eq. (5.2). These three materials can be used only for substrate in waveguide computations.

6 Electron, Hole, and Impurity Statistics

Throughout the model, Fermi-Dirac statistics is used for concentration of electrons, holes, and ionized impurities.

6.1 Electron Concentration

Zinc-Blende Materials Generally, electron concentration includes contributions of Γ, X, and L valleys

$$n = n^{\Gamma} + n^{X} + n^{L} \quad . \tag{6.1}$$

Electron concentration in Γ-valley is given by

$$n^{\Gamma} = N_C^{\Gamma} F_{1/2}\left(\frac{F_n - \left(E_C^{\Gamma} - q\varphi\right)}{kT}\right) \qquad N_C^{\Gamma} = 2\left(\frac{m_{\Gamma} kT}{2\pi\hbar^2}\right)^{3/2} \tag{6.2}$$

where $F_{1/2}$ is Fermi integral of order $1/2$

$$F_{1/2}(t) = \frac{2}{\sqrt{\pi}} \int_{-\infty}^{\infty} \frac{\sqrt{x}\, dx}{1 + \exp(x - t)} \tag{6.3}$$

and N_C^{Γ} is the concentration of states associated with Γ-valley.

Both X and L valleys consist of several conduction band minima with anisotropic effective mass, m_l and m_t, which correspond to direction along the wave vector directed from Γ point and along the plane normal to this direction, respectively. Concentration of states associated with a single minimum of is

$$N_C^{X,L} = 2\left(\frac{m_{av}^{X,L} kT}{2\pi\hbar^2}\right)^{3/2} \tag{6.4}$$

where averaged electron effective mass is $m_{av}^{X,L} = \left(m_l^{X,L}\left(m_t^{X,L}\right)^2\right)^{1/3}$. Strain may cause different energy shift of conduction band minima located at different directions. Respective corrections $\pi_{ijk}^{X,L}$ are given in general form in Eqs. (3.8, 3.9) and particular cases are discussed in Eqs. (3.10-3.12).

There are 6 conduction band minima corresponding to X-valley. They are located completely inside the first Brillouin zone along crystal directions [100], [011], [001], and 3 opposite directions. Electron concentration in X-valley is given by

$$n^{X} = 2N_C^{X} \sum_i F_{1/2}\left(\frac{F_n - \left(E_C^{X} + \pi_i^{X} - q\varphi\right)}{kT}\right) \quad , \quad i = [001], [010], [100] \quad . \tag{6.5}$$

Factor 2 is due to contribution of three opposite directions. Equation (6.5) can be simplified for particular growth directions as following

$$n^{X} = N_C^{X} \begin{cases} 4F_{1/2}\left(\dfrac{F_n - \left(E_C^{X} + \pi_{100}^{X} - q\varphi\right)}{kT}\right) + 2F_{1/2}\left(\dfrac{F_n - \left(E_C^{X} + \pi_{001}^{X} - q\varphi\right)}{kT}\right) & , \quad [001] \\ 2F_{1/2}\left(\dfrac{F_n - \left(E_C^{X} + \pi_{100}^{X} - q\varphi\right)}{kT}\right) + 4F_{1/2}\left(\dfrac{F_n - \left(E_C^{X} + \pi_{001}^{X} - q\varphi\right)}{kT}\right) & , \quad [011] \\ 6F_{1/2}\left(\dfrac{F_n - \left(E_C^{X} + \pi_{100}^{X} - q\varphi\right)}{kT}\right) & , \quad [111] \end{cases} \tag{6.6}$$

There are 8 conduction band minima corresponding to L-valley located along directions [111], [-111], [-1-11], [1-11], and 4 opposite directions. The minima are located at the faces of the first Brillouin zone so only half of the states around each minimum is inside the first Brillouin zone. Similarly to Equations (6.5, 6.6), electron concentration in L-valley is given by

$$n^L = N_C^L \sum_i F_{1/2}\left(\frac{F_n - \left(E_C^X + \pi_i^L - q\varphi\right)}{kT}\right) \quad , \quad i = [111], [-111], [-1-11], [1-11] \quad . \tag{6.7}$$

and can be simplified for particular growth directions as following

$$n^L = N_C^L \begin{cases} 4F_{1/2}\left(\dfrac{F_n - \left(E_C^L + \pi_{111}^L - q\varphi\right)}{kT}\right) & , \quad [001] \\ 2F_{1/2}\left(\dfrac{F_n - \left(E_C^L + \pi_{111}^L - q\varphi\right)}{kT}\right) + 2F_{1/2}\left(\dfrac{F_n - \left(E_C^L + \pi_{1-11}^L - q\varphi\right)}{kT}\right) & , \quad [011] \\ 1F_{1/2}\left(\dfrac{F_n - \left(E_C^L + \pi_{111}^L - q\varphi\right)}{kT}\right) + 3F_{1/2}\left(\dfrac{F_n - \left(E_C^L + \pi_{1-11}^L - q\varphi\right)}{kT}\right) & , \quad [111] \end{cases} \tag{6.8}$$

Wurtzite Materials Both AlInGaN and CdMgZnO alloys have direct energy gap for any composition. We can neglect contributions of X and L valleys because their energy is much higher than conduction band minimum located at Γ valley. So, electron concentration is calculated as

$$n = N_C\, F_{1/2}\left(\frac{F_n - (E_C - q\varphi)}{kT}\right) \qquad N_C = 2\left(\frac{m_{av}^e kT}{2\pi\hbar^2}\right)^{3/2} \tag{6.9}$$

where averaged electron effective mass is $m_{av}^e = \left(m_z^e \left(m_t^e\right)^2\right)^{1/3}$.

6.2 Hole Concentration

Hole concentration is a sum of hole concentrations in each subband

$$p = p_{hh} + p_{lh} + p_{sh} \qquad , \tag{6.10}$$

which are calculated independently

$$p_\nu = N_V^\nu\, F_{1/2}\left(\frac{(E_V^\nu - q\varphi) - F_p}{kT}\right) \quad , \quad N_C^\nu = 2\left(\frac{m_{av}^\nu kT}{2\pi\hbar^2}\right)^{3/2} \quad , \quad \nu = hh, lh, sh \quad . \tag{6.11}$$

For zinc-blende materials, we assume hole masses to be isotropic, so $m_{av}^\nu = m^\nu$. For wurtzite materials, hole masses are averaged over the direction similarly to electron masses $m_{av}^\nu = \left(m_z^\nu \left(m_t^\nu\right)^2\right)^{1/3}$. Calculation of the effective hole masses is described in Secs. (3.4, 4.2).

6.3 Ionized Donors and Acceptors

The concentrations of ionized donors N_D^+ and acceptors N_A^- are related to the total impurity concentrations N_D and N_A as

$$N_D^+ = \frac{N_D}{1 + g_D \exp\left(\dfrac{F_n - (E_C^{min} - q\varphi - E_D)}{kT}\right)}$$
$$N_A^- = \frac{N_A}{1 + g_A \exp\left(\dfrac{(E_V^{max} - q\varphi + E_A) - F_p}{kT}\right)} \tag{6.12}$$

Here, E_C^{min} is the minimum of all valleys of the conduction band, E_V^{max} is the maximum of all subbands of valence band, E_D and E_A are the activation energies of electrons and holes, respectively, while g_D and g_A are the degeneracy factors for impurity energy levels with default values of 2 and 4, respectively.

6.4 Quantum Potential Model

When quantum potential model is turned on, all equations in this section are modified as following. The spatial variation of the band edge profiles, $E_C - q\varphi$ and $E_V - q\varphi$, are replaced by the quantum potentials for electrons and holes accounting for their wave nature (spatial delocalization). Each valley of conduction band and each subband of the valence band are replaced by their own quantum potential (because their effective masses are different).

$$\left[E^\nu - q\varphi\right]_{eff}(z) = \int_{-\infty}^{\infty} \left[E^\nu(z') - q\varphi(z')\right] G(z - z')\, dz' \quad , \quad \nu = \Gamma, X, L, hh, lh, sh \tag{6.13}$$

where $G(t)$ is the Gaussian function and σ_ν is the typical length related to the width of the wave pocket for the carrier type ν

$$G(t) = \frac{1}{2\sigma_\nu\sqrt{\pi}} \exp\left(-\frac{t^2}{4\sigma_\nu^2}\right) \qquad , \qquad \sigma_\nu = \gamma_\nu \sqrt{\frac{\hbar^2}{8m^\nu kT}} \tag{6.14}$$

Here, m^ν is the effective mass for carriers of type ν and γ_ν is the correction factor which can be manually adjusted by the user (default value is 0.7 for electrons and 1 for holes). Note that $G(t)$ becomes delta function when the correction factors tends to zero. However, from computational point of view, it is better to switch off the quantum potential model instead of setting very small correction factors.

7 Carrier Recombination

The total recombination rate R is given by

$$R = R^{rad} + R^{SRH} + R^{Auger} + R^{stim} \tag{7.1}$$

where R^{rad} and R^{Auger} are the radiative recombination rate and Auger recombination rate, while R^{SRH} is the total rate of the non-radiative Shockley-Read-Hall recombination due

to all types of the defect levels in the heterostructure. Dislocations seem to be important channel of the non-radiative recombination in III-nitride materials, and the dislocation-mediated recombination is described within the model developed in [3]. The stimulated recombination rate R^{stim} is included into the model only for simulation of lasers, as discussed in Sec. 11.4. Thermal carrier generation is included into the recombination rate by using the following factor

$$\left[1 - \exp\left(-\frac{F_n - F_p}{k\,T}\right)\right] \qquad .$$

7.1 Radiative Recombination

The rate of bimolecular radiative recombination of electrons and holes is defined by the expression

$$R^{rad} = n^{\Gamma}\left(\sum_{\nu=hh,\,lh,\,sh} B^{\nu}\,p^{\nu}\right)\left[1 - \exp\left(-\frac{F_n - F_p}{k\,T}\right)\right] \tag{7.2}$$

where n^{Γ} is the electron concentration in Γ valley, p^{ν} is the hole concentration for the subband ν.

7.1.1 Radiative Recombination Constant B

The radiative recombination constant B is specified in material properties and there are three options here: (i) constant value for materials and linear interpolation for alloys, (ii) user-defined function, and (iii) parameterization, i.e. calculating B from other material parameters as following

$$B^{\nu} = \frac{2\alpha n_{ref}}{3\hbar}\,\frac{E_G^{\Gamma}\,E^P}{m_0 c^2}\,\frac{1}{N_{rad}^{\nu}} \qquad , \qquad N_{rad}^{\nu} = 2\left(\frac{\left(m^{\Gamma} + m^{\nu}\right)kT}{2\pi\hbar^2}\right)^{3/2} \tag{7.3}$$

where α is the fine-structure constant, n_{ref} is the refractive index, E^P is Kane's matrix element, and factor N_{rad}^{ν} is calculated similarly to the density of states.

By default, the parameterization (7.3) is used for zinc blende materials, while for wurtzite III-nitrides user-defined functions are introduced which implement only the temperature dependence $B\,(T) = B(300K)\,(T/\,300)^{-3/2}$.

Alternatively, users can specify the constant B directly by using options (i) or (ii). In this case, the same value will be used for all subbands of the valence band and no temperature dependence will be included automatically. The temperature dependence of B can be introduced by a user-defined script function, in the way it is done for wurtzite III-nitrides in the default dataset.

7.2 Stimulated Recombination

The stimulated recombination rate is included into the model only for laser computations, and it is assumed to occur only in the quantum wells. Within the well, the stimulated recombination rate is assumed to be proportional to the radiative recombination rate

$$R^{stim} = \begin{cases} \beta R^{rad} & , \text{ inside QWs} \\ 0 & , \text{ outside QWs} \end{cases} \tag{7.4}$$

where factor β is determined iteratively as discussed in Sec. 11.4.

7.3 Shockley-Read-Hall Recombination

Non-radiative recombination caused by deep levels is considered within the Shockley-Read-Hall approach [4]

$$R^{SRH} = \left(\frac{\tau_n^{tot}}{n} + \frac{\tau_p^{tot}}{p} \right)^{-1} \left[1 - \exp\left(- \frac{F_n - F_p}{k\,T} \right) \right] \tag{7.5}$$

where the overall carrier lifetimes, τ_n^{tot} and τ_p^{tot}, include contributions of the dislocations and other defects

$$\tau_{n,p}^{tot} = \left(\frac{f_{n,p}}{\tau_{n,p}^{dis}} + \frac{1}{\tau_{n,p}^{def}} \right)^{-1} \quad . \tag{7.6}$$

The carrier lifetimes due to defects other than dislocations, $\tau_{n,p}^{def}$, are specified directly by the user, while carrier lifetimes related to the dislocations, $\tau_{n,p}^{dis}$, are calculated following the model suggested in [3]

$$\tau_{n,p}^{dis} = \frac{1}{4\,\pi\,D_{n,p}\,N_{dis}} \left(\ln\left(\frac{1}{\pi\,a^2\,N_{dis}} \right) - \frac{3}{2} + \frac{2D_{n,p}}{a\,V_{n,p}} \right) \quad . \tag{7.7}$$

Here, N_{dis} is the dislocation density, $D_{n,p}$ is the diffusion coefficient of electrons or holes, a is the in-plane lattice constant (radius of a dislocation core), $V_{n,p}$ is the carrier thermal velocity.

In (7.6), the factor $f_{n,p}$ comes from the model of the composition fluctuations and describes the fraction of the delocalized carriers (electrons or holes) taking part in the non-radiative recombination at the dislocation cores. These values are calculated according to Eq.(7.8), as discussed below. Please note that $f_{n,p} = 1$ if the composition fluctuation model is not used.

7.3.1 Model of Indium Composition Fluctuations in InGaN QWs

There are various explanations why InGaN QWs show high internal quantum efficiency (IQE) in spite of the high density of threading dislocations inherent in III-nitride epitaxial materials. One hypothesis is that fluctuations of InGaN composition may increase IQE by capturing carriers in local indium-rich regions and preventing these carriers from reaching dislocations. Such carriers are considered as localized, while other ones are regarded to be capable of easily moving in the active layer and reaching centers of the non-radiative SRH recombination. A special model is available in SiLENSe to account for this effect.

Let us denote the fraction of delocalized electrons and holes, which are not captured by indium-rich regions and so can recombine at dislocations, as $f_n\left(\Phi_n, U_n\right)$ and $f_p\left(\Phi_p, U_p\right)$, respectively, where $\Phi_n = F_n - E_C + q\varphi$ and $\Phi_p = E_V - q\varphi - F_p$. Parameters U_n and U_p characterize statistical distributions of the energy levels in the conduction and valence bands, assuming exponential tails of density of states inside the bandgap. Equation (7.6) includes the fraction of the delocalized carriers participating in the dislocation recombi-

nation which is calculated as

$$f\left(\Phi,U\right)=\begin{cases}\dfrac{k\,T}{U+k\,T}\;\cdot\;\dfrac{\ln\left(1+\exp\left(\Phi/kT\right)\right)}{\ln\left(1+\exp\left(\dfrac{\Phi}{U+k\,T}\right)\right)} & ,\quad \Phi<0\\ 1-\dfrac{U}{U+k\,T}\;\cdot\;\dfrac{\ln 2}{\ln\left(1+\exp\left(\dfrac{\Phi}{U+k\,T}\right)\right)} & ,\quad \Phi\geq 0\end{cases} \tag{7.8}$$

The latter expression is derived in a manner used previously for analysis of the emission spectra from InGaN quantum wells [5].

7.4 Auger Recombination

Auger recombination is given by

$$R^{Auger}=\left(C_n\,n^{\Gamma}n^{\Gamma}\,p+C_p\,n^{\Gamma}\,p^2\right)\left[1-\exp\left(-\frac{F_n-F_p}{k\,T}\right)\right] \tag{7.9}$$

where n^{Γ} is the electron concentration in Γ valley, while C_n and C_p are Auger recombination coefficients.

7.4.1 Auger coefficient C_n

For Auger recombination process involving two electrons in Γ valley and one heavy hole, the recombination constant can be calculated as [6]

$$C_n^{CHCC}=\frac{24Ry^*}{\pi^{1/2}\hbar\chi_1^{1/2}\chi_2^{3/2}N_C^{\Gamma}N_V^{hh}}\left(\frac{kT}{E_G^{\Gamma}}\right)^{5/2}\exp\left(-\frac{E_{th}}{kT}\right) \tag{7.10}$$

where

$$E_{th}=\frac{m^{\Gamma}}{m^{hh}}\chi_1\chi_2E_G^{\Gamma}\quad,\quad \chi_1=\frac{2E_G^{\Gamma}+\Delta}{3E_G^{\Gamma}+\Delta}\quad,\quad \chi_1=\frac{3E_G^{\Gamma}+2\Delta}{E_G^{\Gamma}+\Delta}$$

Here, m^{Γ} and m^{hh} are the effective masses of electrons in Γ valley and of heavy holes, E_G^{Γ} and Δ are the direct energy gap and spin-orbital splitting, N_C^{Γ} and N_V^{hh} are the concentrations of states for electrons in Γ valley and for heavy holes (see Sec. 6), and

$$Ry^*=\frac{m^{\Gamma}}{m_0\,\varepsilon^2}\,13.61\;eV$$

is the effective Rydberg energy for electron.

Parameterization (7.10) works fine for energy gap below $\sim 1.2\,eV$, or for the C_n parameter higher than $\sim 10^{-30}cm^{-6}s^{-1}$. For higher energy gaps, the experimentally observed Auger recombination coefficient does not further decline exponentially with the energy gap. The detailed microscopic mechanism of the Auger process in wide-bandgap semiconductors is not determined clearly, and even indirect-gap materials follow this trend [7].

So, the final equation for C_n coefficient is

$$C_n=\max\left\{C_n^{CHCC}\quad,\quad C_n^{min}\right\} \tag{7.11}$$

where C_n^{min} is an additional material parameter which user can specify individually for any material or alloy. This approach allows to treat in the same way alloys with a large variation of the energy gap, say InGaAs.

Setting "Paramerization" option for the Auger coefficient C_n means that Eq. (7.11) will be used to calculate it. Alternatively, C_n can be specified directly by user, as any other material parameter. Because of its complicated dependence on the band structure and temperature, very probably, one will need write a user-defined script function for it.

7.4.2 Auger coefficient C_p

For Auger processes involving one electron and two holes, the Auger coefficient dramatically depends on the details of the band structure, especially if the hole transitions between different subbands play an important role. It becomes impossible to describe a wide range of material composition with the same equation. So, the default value of C_p is zero, and users are welcome to modify its value according to the particular material compositions they are dealing with.

8 Drift-Diffusion Model

Drift-diffusion model is used for coupled simulation of the electric potential and carrier transport in the heterostructure. From mathematical point of view, drift-diffusion model is a set of three second order differential equations. First one is Poisson equation for the electric potential, the other two are transport equations for electrons and holes. Solving Equations (8.1) and (8.4) self-consistently is the key procedure for computation of the band diagram, carrier concentration, current density and some other results provided by SiLENSe.

8.1 Electric Potential Distribution

The Poisson equation is employed for computation of the electric potential $\varphi(z)$ in the heterostructure:

$$\frac{d}{dz}\left(k_0 k^* \frac{d\varphi}{dz} - P_z^{tot}\right) = -q\left(p - n + N_D^+ - N_A^-\right) \tag{8.1}$$

where q is the magnitude of the electron charge, k_0 is the dielectric permittivity of vacuum, and k^* is the effective static dielectric constant in the direction normal to the epilayers given by Eq. (2.18).

8.2 Carrier Transport

Within the drift-diffusion model, the current density associated with electrons and holes is assumed to be proportional to the gradient of the Fermi level for the respective carriers

$$j_n = n\,\mu_n\,\frac{dF_n}{dz} \qquad , \qquad j_p = p\,\mu_p\,\frac{dF_p}{dz} \tag{8.2}$$

Under steady state conditions, the continuity equation for carriers reads as

$$\frac{d\,j_n}{dz} = q\,(R - G) \qquad , \qquad \frac{d\,j_p}{dz} = -q\,(R - G) \tag{8.3}$$

where R is the carrier recombination rate and G is the carrier generation rate caused by photoexcitation which differs from zero only for the photoluminescence simulations described in Sec. (12). Substitution of (8.2) into (8.3) yields second order equations for the Fermi levels

$$\frac{d}{dz}\left(n\,\mu_n\,\frac{dF_n}{dz}\right) = q\,(R-G) \qquad , \qquad \frac{d}{dz}\left(p\,\mu_p\,\frac{dF_p}{dz}\right) = -q\,(R-G) \tag{8.4}$$

Together with (8.1), these equations form the drift-diffusion model widely used in simulation of semiconductor devices.

8.3 Boundary conditions

As all three variables, electric potential and two Fermi levels, have physical meaning of energy, there is a freedom of choosing the reference point. In SiLENSe, the reference point for the carrier energy is the electron Fermi level at n-side, while hole Fermi level at the p-side depends on the p-n junction bias U_b applied to the structure.

$$\begin{cases} F_n &= 0 \quad , \quad (n-side) \\ F_p &= -U_b \quad , \quad (p-side) \end{cases} \tag{8.5}$$

The electric potential at the boundaries of the heterostructure is determined from the condition of charge neutrality

$$\begin{cases} N_D^+ &= n \quad , \quad (n-side) \\ N_A^- &= p \quad , \quad (p-side) \end{cases} \tag{8.6}$$

Minority carriers are assumed to be emitted into the metallic Ohmic contacts with Richardson velocity, that provides us the boundary condition for the current density of the minority carriers

$$j_n = q\,n\,v_R^n \qquad (n-side) \qquad , \qquad j_p = q\,p\,v_R^p \qquad (p-side) \tag{8.7}$$

where Richardson velocity is

$$v_R^{n,p} = \sqrt{\frac{k\,T}{2\,\pi\,m_{av}^{n,p}}} \qquad . \tag{8.8}$$

9 Characteristics of LED Heterostructure

9.1 Internal Quantum Efficiency and Injection Efficiency

One of the most important characteristics of an LED structure is the internal quantum efficiency (IQE). In SiLENSe, IQE is calculated as the ratio of the current density converted to the radiative recombination from the QW layers to the total current density

$$IQE = \frac{q}{j}\int_{QW} R^{rad}(z)\,dz = j_{QW}^{rad}/\,j \qquad where \qquad j_{QW}^{rad} = q\int_{QW} R^{rad}(z)\,dz \tag{9.1}$$

With such definition of IQE, it is the only integral parameter describing efficiency of the structure, combining both (i) competition between radiative and non-radiative

recombination and (ii) carrier injection/leakage. The external quantum efficiency (EQE) of an LED chip is $EQE = IQE \times LEE$ where LEE is the light extraction efficiency.

The injection efficiency is the ratio of the total current density converted into recombination in the QW layers to the total current density

$$\eta^{inj} = \frac{q}{j} \int_{QW} R(z)\, dz = j_{QW}^{rec} / j \qquad where \qquad j_{QW}^{rec} = q \int_{QW} R(z)\, dz \tag{9.2}$$

Injection efficiency is often used to quantify the carrier injection into the active region (or, in other words, the carrier leakage).

Note that in literature there is an alternative definition of the internal quantum efficiency where it describes only competition between radiative and non-radiative recombination

$$IQE' = j_{QW}^{rad} / j_{QW}^{rec} \tag{9.3}$$

One can see that $IQE = IQE' \times \eta^{inj}$ and $EQE = IQE' \times \eta^{inj} \times LEE$.

9.2 Estimation of I-V Characteristic of an LED Chip

SiLENSe implements 1D simulations and computes the current density j as a function of p-n junction bias U_b which is lower than the total voltage V applied to the LED chip. Normally, LED chips have some series resistance due to lateral current spreading and contact resistance. The series resistance cannot be estimated within the 1D approach. However, if the series resistance is known experimentally, it becomes possible to estimate the actual I-V characteristic of the chip. Let the dependence $j(U_b)$ to be known from SiLENSe simulations. Then the total voltage V and the electric current I can be estimated as

$$I = jA \qquad , \qquad V = U_b + IR_s \tag{9.4}$$

where A is the active region area and R_s is the series resistance.

9.3 Other Parameters

As the $j(U_b)$ characteristic is computed, the non-ideality factor is calculated as

$$m_i = \frac{U_b^{(i)} - U_b^{(i-1)}}{kT \log\left(j^{(i)} / j^{(i-1)}\right)} \tag{9.5}$$

where indices i and $i-1$ denote values for two consecutive results.
The total sheet concentrations of the carriers in the active region are calculated as

$$n^{2D} = \int_{QW} n(z)\, dz \qquad , \qquad p^{2D} = \int_{QW} p(z)\, dz \tag{9.6}$$

These values are used later in SpeCLED in the post-processing computation of lateral carrier diffusion in the active region and non-radiative recombination at the active region sidewalls.

10 Light Emission Spectrum and Gain Spectrum

10.1 Overview of Spectrum Computation

Calculation of the light emission spectra includes the only but principal channel – radiative recombination between the electron and hole states confined in the quantum-well active region. Other important channels involving, for instance, the recombination of free carriers and of the carriers captured by donors and acceptors are ignored in the current version of the software. The optical module employs the Schrödinger equations for electrons and holes with the potential energy determined from a self-consistent solution of the Poisson and drift-diffusion transport equations considered in Sec. (8). Calculation of the spontaneous emission spectrum and gain spectrum includes the following steps which are processed independently for each quantum well (QW):

- determination of the computational domain for Schrödinger equation which includes the QW and some region around it and generation of the computational mesh in the domain;
- solution of the Schrödinger equation for electrons and holes which provides carrier energy levels and wave functions;
- calculation of the spontaneous emission spectrum and gain spectrum for each pair of electron and hole energy levels in the QW;
- summation over all the pairs of electron and hole energy levels in the QW.

Finally, contributions of all QWs are combined together to get the final spectrum. Note that the detailed information about contribution of each pair of electron and hole energy levels is also stored during the computation and presented to users in the "Detailed Spectrum" window.

The above steps will be discussed in detail in the next sections.

10.2 Schrödinger Equation for Electrons and Holes

In computation of the emission spectrum, three types of holes (heavy, light, and split-off) are considered independently, and splitting of the valence band is discussed in Secs. (3) and (4) for zinc-blende and wurtzite materials, respectively. 1D Schrödinger equation for energy levels E and wave functions Ψ for electrons and holes is

$$-\frac{\hbar^2}{2m_\perp^e}\frac{d^2\Psi}{dz^2}+U_C^{eff}\Psi=E\Psi \qquad , \qquad \frac{\hbar^2}{2m_\perp^\nu}\frac{d^2\Psi}{dz^2}-U_{V_\nu}^{eff}\Psi=E\Psi \tag{10.1}$$

Here, $\nu = hh, lh, sh$ is the hole type, $m_\perp^e$ and $m_\perp^\nu$ are the carrier effective masses in the direction normal to the epilayers, U_C^{eff} and $U_{V_\nu}^{eff}$ are the effective QW profiles for electrons and holes of type ν. For zinc blend materials, the effective masses are assumed to be isotropic, while for wurtzite materials the effective masses in the direction normal to the epilayers and parallel to the epilayers depend on the inclination angle θ between the [0001] direction of the crystal and normal to the epilayers

$$m_\perp=\left(\frac{\sin^2\theta}{m_t}+\frac{\cos^2\theta}{m_z}\right)^{-1} \qquad , \qquad m_\parallel=\left(\frac{\cos^2\theta}{m_t}+\frac{\sin^2\theta}{m_z}\right)^{-1/2} m_t^{1/2} \tag{10.2}$$

Note that for non-zero θ the effective mass in the direction parallel to the epilayers is anisotropic, and $m_{\|}$ is an averaged effective mass used to calculate 2D density of states.

First kind boundary conditions ($\Psi = 0$) are used at both boundaries of the computational domain for the Schrödinger equation (10.1). For correct computation of the energy levels and wave functions in the QW, we need include into the computational domain for the Schrödinger equation the barrier layers surrounding the QW. Besides, if the barrier layers are not so thick, we need include into the computational domain the distance larger than the thickness of the barrier layer and, in case of MQWs, ignored the adjacent QWs (as we consider all QWs independently). That is why we need introduce an effctive potential profile of the QW which is used in Eq. (10.1).

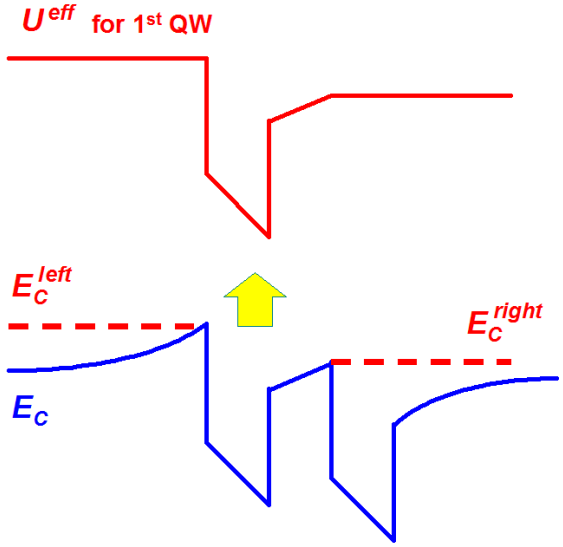

Figure 1: Generation of the effective QW profile for electrons.

The computational domain for the Schrödinger equation and effective potential profile for electrons are determined by the below procedure illustrated in Fig. 1.

- Inside the QW, i.e. for the layers marked as QW layers by the user, the effective QW profile equals to the profile of the respective band.

- Starting from the right boundary of the QW, we move right cell by cell and assign the effective QW profile as following

$$U_C^{eff}(z_i) = max\left\{E_C(z_i) - q\varphi(z_i) \quad , \quad U_C^{eff}(z_{i-1})\right\}$$

  Here, z_i and z_{i-1} mean the centers of cells i and $i-1$, respectively. Such definition of the effective potential avoid possible appearance of artificial localized states located in minimuma of the conduction band outside the current QW.

- The next task is to determine how long should be the computational domain right to the QW. It is controlled by two solver parameters called "Minimum energy level" and "Wave function damping in the barrier" with the default parameters of 20 meV and 100, respectively. We introduce the "top energy" of the QW by taking minimum height of the barriers at the QW boundaries and subtracting the "Minimum energy

level" value. Then we calculate how the quasi-classical wave function of an electron with this energy will damp as we go right from the QW boundary. We stop moving right when the wave functions damps by a factor greater than value of the "Wave function damping in the barrier" parameter. So, we ensure that all energy levels we will compute by numerical solution of Eq. (10.1) with an energy lower than "top energy" will damp by the factor greater than "Wave function damping in the barrier" parameter.

- The effective QW profile and boundary of the computational domain left to the QW are determined in the similar way.

- For holes, the procedure is similar, but the sign of all energies is inverted.

Performing the above procedure for electrons and 3 types of holes, we obtain 4 different computational domains. Then we join them together to have the same computational domain for all 4 types of carriers. The necessary extrapolation of the effective QW profile is done similarly to the procedure described above.

Finally, Eq. (10.1) is solved numerically, and localized energy levels and the respective wave functions are computed.

10.3 Spontaneous Emission Spectrum

Below, we will describe calculation of the spontaneous emission spectrum of an individual quantum well. For MQW structures, the total spectra are obtained by summation of contributions of individual QWs. Contribution of a transition between i-th electron level and j-th hole level of the subband ν to the spontaneous emission is calculated as

$$\begin{aligned} w_{spont}^{i,\nu,j}(\omega) &= \frac{2\pi}{\hbar}\left(\frac{q}{m_0 c}\right)^2 |A_0|^2 |P_h|^2 \left|\langle \Psi_i^e \mid \Psi_j^\nu \rangle\right|^2 \times \\ &\times \int \frac{\mathbf{d^2 k}}{2\pi} f_i^e(\mathbf{k}) f_j^\nu(\mathbf{k}) \delta\left(\hbar\omega - \left(E_i^e - E_j^\nu\right) - \frac{\hbar^2 k^2}{2\mu_\parallel}\right) \eta_{fluct}^{i,\nu,j}(\omega) \end{aligned} \quad (10.3)$$

where m_0 is the electron mass in vacuum, c is the light velocity in vacuum, $|A_0|^2$ the magnitude of the vector potential normalized to one photon in the unit volume, $|P_h|^2$ is the squared interband momentum matrix element for subband ν averaged over the photon directions, $\left|\langle \Psi_i^e \mid \Psi_j^\nu \rangle\right|^2$ is the squared overlap integral between the electron and hole wave functions (for 1D case, it is always possible to choose real wave functions), the integration is done over the in-plain wave vector k, and δ denotes the Dirac delta function. The distribution functions f represent the probability that the state with wave vector $\mathbf{k}$ is occupied by the carrier

$$\begin{aligned} f_i^e(\mathbf{k}) &= \left[1 + \exp\left(\left(E_i^e + \frac{\hbar^2 k^2}{2m_\parallel^e} - F_n'\right) \Big/ kT\right)\right]^{-1} \\ f_j^\nu(\mathbf{k}) &= \left[1 + \exp\left(\left(F_p' - E_j^\nu - \frac{\hbar^2 k^2}{2m_\parallel^\nu}\right) \Big/ kT\right)\right]^{-1} \end{aligned} \quad (10.4)$$

where F_n' and F_p' are corrected electron and hole Fermi levels (see the next section for more details). The factor

$$\eta_{fluct}^{i,\nu,j}(\omega) = \left(1 + \exp\left(\frac{E_i^e - E_j^\nu - \hbar\omega}{U_{sp}}\right)\right)^{-1} \tag{10.5}$$

represents the reduced density of states modified by the composition fluctuations which supposed to modify randomly the energy gap of the QW material and, therefore, the difference between the electron and hole energy levels. The user-defined parameter U_{sp} specifies the typical energy of the reduced DOS tail into the energies below the value of $E_i^e - E_j^\nu$. Equation (10.5) resembles the Fermi distribution function and in case of $U_{sp} \to 0$ it tends to the Heaviside step function $\eta_{fluct}^{i,\nu,j}(\omega) = \Theta\left(\hbar\omega - \left(E_i^e - E_j^\nu\right)\right)$ that is a conventional result for an ideal QW.

The total contribution of the QW is calculated by summation over all pairs of electron and hole energy levels

$$w_{spont}^{tot}(\omega) = C \sum_{\nu\,=\,hh,\,lh,\,sh} \sum_{i,\,j} w_{spont}^{i,\nu,j}(\omega) \tag{10.6}$$

Here, C is a normalization factor chosen in such a way that the total radiative recombination rate computed by integration of the spontaneous emission spectrum is equal to the radiative recombination rate in the QW computed from the main drift-diffusion solution of the carrier transport problem. More detailed discussion on matching classical and quantum approaches can be found in the next section. Here we would like just note that C is usually close to unity, which indicates that correction of the Fermi level, described below, provides a satisfactory matching between the results obtained within the classical and quantum approaches.

10.4 Correction of the Fermi Levels in QWs

There is a problem how to match results obtained within the classical drift-diffusion model applied for computation of the band diagram, Fermi levels, carrier concentration, and so on with the quantum-mechanical consideration used to compute optical characteristics. Particularly, what Fermi levels to be used to calculate the occupancy factors $f_i^e(\mathbf{k})$ and $f_j^\nu(\mathbf{k})$ in Eq. (10.3)? The thing is that if we use the Fermi levels obtained within the classical model with the energy levels computed by solving the Schrödinger equation, we would get a carrier concentration considerably lower that that predicted by the classical model. The reason is the distance between the bottom of the QW profile and the ground carrier energy level.

To make computation of the emission spectrum consistent with the classical results obtained by solution of the drift-diffusion problem, corrected Fermi levels are introduced. The corrected electron Fermi level is determined from the condition that the 2D sheet electron concentration in the QW is the same in both approaches, $n_{quantum}^{2D} = n_{classical}^{2D}$, where 2D concentrations are given by

$$\begin{aligned} n_{classical}^{2D} &= \int_{QW} n(z)\,dz \\ n_{quantum}^{2D} &= \frac{m_\parallel^e kT}{\pi\hbar^2} \sum_i \log\left[1 + \exp\left(\frac{F_n' - E_i^e}{kT}\right)\right] \end{aligned} \tag{10.7}$$

A similar approach is used to correct the hole Fermi level.

10.5 Stimulated Emission and Gain Spectrum

The stimulated emission spectrum is calculated very similar to the spontaneous emission, Eq. (10.3), the difference is only in use of the band-filling factors f

$$\begin{aligned} w_{stim}^{i,\nu,j}(\omega) &= \frac{2\pi}{\hbar}\left(\frac{q}{m_0 c}\right)^2 |A_0|^2 |P_h|^2 \left|\langle \Psi_i^e \mid \Psi_j^\nu \rangle\right|^2 \times \\ &\times \int \frac{\mathbf{d^2k}}{2\pi} \left(f_i^e(\mathbf{k}) + f_j^\nu(\mathbf{k}) - 1\right) \delta\left(\hbar\omega - \left(E_i^e - E_j^\nu\right) - \frac{\hbar^2 k^2}{2\mu_\parallel}\right) \eta_{fluct}^{i,\nu,j}(\omega) \end{aligned} \tag{10.8}$$

The total gain spectrum is calculated by summation over pairs of electron and hole energy levels similarly to spontaneous emission

$$w_{stim}^{tot}(\omega) = \sum_{\nu = hh, lh, sh} \sum_{i,j} w_{stim}^{i,\nu,j}(\omega) \tag{10.9}$$

The optical gain is related to the stimulated emission as

$$g(\omega) = \frac{\pi^2 c^2 \hbar}{n^2 \omega^2} w_{stim}^{tot}(\omega) \tag{10.10}$$

where n is the refractive index. Negative values of stimulated emission rate describe optical absorption.

10.6 Spectrum Broadening

The spectrum broadening is simulated by convolving the calculated emission intensity with broadening function L , which tends to the Dirac delta function when the broadening parameter γ tends to zero.

$$I_{broad}(\omega) = \int_0^\infty I(\omega') L(\omega - \omega') d\omega' \qquad , \qquad L(x) = \frac{1}{2\gamma} \exp\left(-\frac{|x|}{\gamma}\right) \tag{10.11}$$

This approach provides an emission spectrum profile that frequently observed in experiments. The user can adjust the broadening parameter γ according to the experimental data. The above procedure is applied to both spontaneous emission spectrum and gain spectrum.

11 Simulation of Edge-Emitting Lasers

11.1 Waveguide Modes

Wave Equations Let us consider a waveguide mode of TE polarization travelling along the x-axis. The electric field can be written as $\mathbf{E}(x,y,z) = \mathbf{e_y} E_y(z) \exp[\imath(\beta x - \omega t)]$, where $\mathbf{e_y}$ is the unit vector along y-axis and the electric field magnitude E_y obeys the wave equation for the eigenvalues β and eigenfunctions $E_y(z)$

$$\frac{1}{n_t^2}\frac{d^2 E_y}{dz^2} + k^2 E_y = \frac{\beta^2}{n_t^2} E_y \tag{11.1}$$

Here, $n_t(z)$ is the ordinary refractive index and $k = \omega/c$ is the wave vector in vacuum. Below, we will call the ratio β/k as "effective refractive index" for the certain mode. The boundary conditions at the internal interfaces are continuity of E_y and dE_y/dz.

Similarly, the amplitude of TM mode with the magnetic field given by $\mathbf{H}(x,y,z) = \mathbf{e_y} H_y(z) \exp[\imath(\beta x - \omega t)]$, where H_y can be found from the wave equation

$$\frac{d}{dz}\left(\frac{1}{n_t^2}\frac{dH_y}{dz}\right) + k^2 H_y = \frac{\beta^2}{n_z^2} H_y \tag{11.2}$$

where $n_z(z)$ is the extraordinary refractive index.

Boundary Conditions We assume that a thick metallic contact is placed on top of the heterostructure, that results in the following boundary conditions

$$\begin{array}{rrcl} TE: & E_y\big|_{top} & = & 0 \\ TM: & \left.\dfrac{dH_y}{dz}\right|_{top} & = & 0 \end{array} \tag{11.3}$$

The substrate may play an important role in optical confinement (say, sapphire substrate in case of III-nitride structure). So we include in the waveguide computations some part of the substrate. The thickness of substrate included into the computations is much thinner than the total substrate thickness, it just should provide enough optical confinement. Assuming the mode to be confined in the heterostructure and exponentially damping in the substrate, we use the first kind boundary conditions at the bottom of the substrate

$$\begin{array}{rrcl} TE: & E_y\big|_{bottom} & = & 0 \\ TM: & H_y\big|_{bottom} & = & 0 \end{array} \tag{11.4}$$

The condition of exponential damping in the substrate is as following

$$\begin{array}{rrcl} TE: & n_t^{sub} & < & \beta/k \\ TM: & n_z^{sub} & < & \beta/k \end{array} \tag{11.5}$$

where $n_{t,z}^{sub}$ is the refractive index of the substrate. The modes that do not satisfy Eq. (11.5) are called "leaking modes". Formally, they propagate infinitely into the substrate (if we consider the substrate to be a half-space), but in reality they are confined in the structure and the amount of energy going into the substrate decays exponentially with the thickness of the cladding layer(s). The physical meaning of this situation is similar to the case when we put an electron into a QW between two thick barriers, but outside the barriers there are states of continuum spectrum. Formally, the states inside the QW are not "true" localized, as electron have a chance to tunnel outside. While as far as the tunneling time is much longer than typical times of other processes, we can consider such states inside the QW as localized states.

If the substrate has a higher refractive index than the first heterostructure layer, the computations are performed with the substrate refractive index equal to that of the first layer. This approach allows to avoid modes confined in the substrate.

Far Field As the light comes out of the waveguide through the output mirror, its angular distribution depends on the field distribution inside the waveguide. The angular distribution of the far field intensity of TE modes is calculated as

$$I_{TE}(\theta) = \left| \frac{\langle E_y \rangle \cos\theta}{k\cos\theta + \beta} \right|^2 \tag{11.6}$$

where operator $\langle\ \rangle$ is defined as

$$\langle f(z) \rangle = \int_{-\infty}^{\infty} f(z) \exp(-\imath k z \sin\theta)\, dz \tag{11.7}$$

The far field of TM modes is described by a more complicated expression:

$$I_{TM}(\theta) = \left| \frac{\langle H_y \rangle \langle H_y / n_z^2 \rangle \cos\theta}{\langle H_y \rangle k\cos\theta + \langle H_y / n_z^2 \rangle \beta} \right|^2 \tag{11.8}$$

11.2 Optical Gain

The optical gain for the certain mode is given by the expression

$$g = \sum_{QWs} g_i \Gamma_i \tag{11.9}$$

where sum is taken over all quantum wells in the active region, g_i is the gain in i-th quantum well, and Γ_i is the optical confinement factor for this QW which is calculated as

$$\Gamma_i = \int_{z_i}^{z_i+d_i} E_y^2(z)\, dz \Big/ \int_{-\infty}^{\infty} E_y^2(z)\, dz \tag{11.10}$$

Here, z_i and d_i are the position and thickness of i-th quantum well, respectively.

11.3 Optical Losses

The optical loss because of free carrier absorption is given by

$$\alpha^{free} = \int_{-\infty}^{\infty} E_y^2(z)\, \alpha(z)\, dz \Big/ \int_{-\infty}^{\infty} E_y^2(z)\, dz \tag{11.11}$$

where $\alpha = \alpha_n + \alpha_p$ is the sum of the absorption coefficients for electrons and holes

$$\alpha_n = \frac{q^3\lambda^2 n}{4\pi^2 \mu_n m_n^2 n_{ref} \varepsilon_0 c^3} \quad , \quad \alpha_p = \frac{q^3\lambda^2 p}{4\pi^2 \mu_p m_p^2 n_{ref} \varepsilon_0 c^3} \tag{11.12}$$

where n and p are the concentrations of electrons and holes. Here we have neglected the anisotropy of the carrier effective masses $m_{n,p}$, mobilities $\mu_{n,p}$, and refractive index n_{ref}. Optionally, absorption coefficient taken from the dataset of the material properties can be used for calculating absorption in the layers which are not QWs (in QWs, the gain replaces the interband absorption, so absorption from the dataset is not applicable). The total optical absorption is calculated as

$$\alpha^{tot} = \alpha^{free} + \alpha^{rad} + \alpha^{add} \tag{11.13}$$

where α^{add} is a user-defined additional source of optical loss, for instance, waveguide nonideality, and α^{rad} is the radiative loss given by

$$\alpha^{rad} = -\frac{1}{2L_{cav}} \log\left(R_{out} R_{back}\right) \tag{11.14}$$

Here, L_{cav} is the cavity length, and R_{out} and R_{back} are the reflectivities of the output and back mirrors, respectively.

11.4 Laser Characteristics (Self-Consistent Model)

Laser computations within the self-consistent model can be started by using *"Run -> Single Calculation With Laser"* and *"Run -> Series Calculation With Laser"* items of the main menu for single or multiple biases, respectively. The key idea and computation flow are described below in this section.

The conventional rate equations provide the following relation between the stimulated and radiative recombination [10]

$$R^{stim} = 2\,\gamma\,\frac{g}{\alpha^{tot} - g}\,R^{rad} \tag{11.15}$$

where γ is is the coupling coefficient accounting for the fraction of spontaneous emission contributing to the waveguide mode. As the typical values of γ are in range of $10^{-6} \div 10^{-4}$, the fraction in Eq. (11.15) is rather high, i.e. the modal gain approaches the total modal losses with high accuracy. So, we have simplified the above model as following. The stimulated recombination rate R^{stim} equals to the spontaneous radiative recombination rate R^{rad} multiplied by a factor β which is determined iteratively until the condition

$$g = a^{tot} \tag{11.16}$$

is fulfilled with the accuracy prescribed by user (see also 7.2).

The following computations are performed for a certain bias (please also refer the flow chart shown in Fig. 2):

- Computation of the band diagram, carrier concentration, and so on with $\beta = 0$ (like in LED case).
- Computation of the gain spectrum and determination of the peak wavelength. In case of no gain the computation is stopped with zero output laser power.
- Waveguide modes are computed for the gain peak wavelength.
- The optical gain and losses are computed by using the known gain spectrum and distribution of free carriers. Optical gain is compared with the total optical losses. If the gain is lower than the total losses, the computation is stopped with zero output laser power.
- Some non-zero initial guess for β is specified (user can control it, default is 0.05). Then the following steps are repeated automatically until the condition (11.16) is reached:
  - Computation of the band diagram, carrier concentration, etc.

– Computation of the gain spectrum and looking for its peak.
– Computation of the waveguide modes at the gain peak wavelength.
– Computation of the modal gain and total modal losses and comparing them. If their difference is lower than the prescribed accuracy, the computations are stopped. Otherwise, a new approximation for β is calculated.

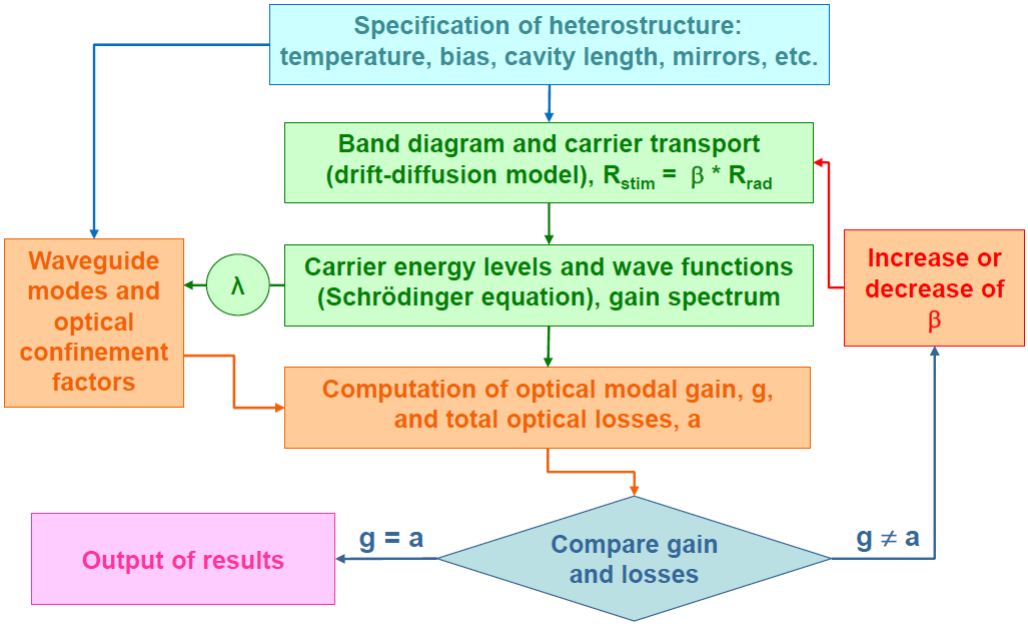

Figure 2: Flow chart for the laser self-consistent model (single bias).

The output laser power is proportional to the stimulated recombination current density and laser area S

$$P^{out} = \hbar\,\omega\,\frac{\alpha^{rad}}{\alpha^{tot}}\,f_R\,S\int_{-\infty}^{\infty} R^{stim}\,(z)\,dz \tag{11.17}$$

where factor f_R describes optical loss at the back mirror (please note that $f_R = 1$ if $R_{back} = 1$):

$$f_R = \frac{1 - R_{out}}{\sqrt{R_{out}}}\,\frac{\sqrt{R_{back}\,R_{out}}}{\left(\sqrt{R_{back}} + \sqrt{R_{out}}\right)\left(1 - \sqrt{R_{back}\,R_{out}}\right)} \tag{11.18}$$

NB Above definition of the output power describes the laser power going out only through the output mirror. The light going out through the back mirror (if any) is considered to be useless and do not contribute to the output power.

11.5 Laser Characteristics (Simplified Model)

To speed up determination of laser threshold current, a simplified model can be used. First, one needs do drift-diffusion simulation for a range of bias/current in the same way it is done for LED structures, i.e. use *"Run -> Single Calculation"* or *"Run -> Series Calculation"* items of the main menu or the respective buttons in the toolbar. Second, one needs use *"Run -> Laser Characteristics (Simplified Model)"* item of the main menu which will perform the following computations for all LED results which are included in the project file:

- Computation of the gain spectrum and determination of the peak wavelength. In case of no gain the computation for this bias is stopped with zero output laser power and next bias is processed.
- Waveguide modes are computed for the gain peak wavelength.
- The optical gain and losses are computed by using the known gain spectrum and distribution of free carriers. Optical gain is compared with the total optical losses.
- If the gain is lower than the total losses, the computation is stopped with zero output laser power and next bias is processed. So, the below steps are processed only if the gain is higher than the total losses.
- If it is the first bias for which gain is higher than losses, a linear interpolation of all results (bias, current density, gain, losses, etc.) is done in between this bias and previous bias, and the threshold current and other parameters at the threshold are determined from the condition that gain and losses are equal.
- Laser output power is calculated according to Eq. (11.19) below.

Within the simplified model, we assume that laser output power linearly increases with the operating current

$$P^{out}_{simple} = (j - j_{th})\, S\eta \tag{11.19}$$

Here, j_{th} is the threshold current density, and below subscript "th" will denote value at the threshold. The differential efficiency η is calculated as

$$\eta = \frac{\hbar\,\omega}{q}\,\frac{\alpha^{rad}_{th}}{\alpha^{tot}_{th}}\,\eta^{inj}_{th}\,f_R \tag{11.20}$$

where η^{inj}_{th} is the injection efficiency at the threshold and other parameters are similar to Eq. (11.17). Here, we assume that all the additional (compared to the threshold) current density injected into the active region is distributed between the recombination in the active region and leakage according to η^{inj}_{th} value, and that all the additional recombination in the active region is the stimulated emission.

NB Prediction of the threshold current works exactly in the same way for self-consistent and simplified models. However, the simplified model works several times faster, because it does drift-diffusion computation once only, while the self-consistent model does drift-diffusion computations several times to find β factor iteratively.

NB Prediction of the laser output power works differently for self-consistent and simplified models. The difference is that in self-consistent model we include stimulated recombination into the drift-diffusion model and do computations self-consistently, while in the simplified model we just introduce a factor of η^{inj}_{th} in Eq. (11.20) for the differential efficiency and output power.

12 Photoluminescence

Software enables simulation of the steady-state photoluminescence (PL) experimental setup within the following approach. Prior to the main computations, the generation rate caused by PL excitation is calculated as discussed below. The main drift-diffusion

computations are performed as for LED operation with the generation rate included into the carrier transport equations (8.4). Finally, the PL emission spectrum is calculated in the manner similar to that for LED simulations. The PL mode can also be used to simulate operation of photodiodes and single-junction solar cells.

The PL excitation is assumed to be monochromatic. The user specifies the excitation wavelength and power density, as well as direction of the excitation, i.e. from top or bottom side of the structure. Let us denote the total number of layers as N, and they form N+1 boundaries enumerated from 0 (top heterostructure surface) to N (bottom heterostructure surface). The user specifies energy reflection coefficients R_0 and R_N at the top and bottom surfaces, respectively. Another option is to specify the refractive index of the immersion medium n_{out} (default is 1), and the reflection coefficients are automatically calculated as

$$R_0 = \left(\frac{n_{out} - n_1}{n_{out} + n_1}\right)^2 \qquad , \qquad R_N = \left(\frac{n_{out} - n_N}{n_{out} + n_N}\right)^2 \tag{12.1}$$

where n_1 and n_N are the refractive indices of the top and bottom layers, respectively.

Let us assume that incident light comes to the top surface with the reflectivity R_0, as shown in Fig. 3. Otherwise, one needs just interchange R_0 and R_N in the rest of this chapter. Let $I^{(+)}(z)$ and $I^{(-)}(z)$ be the excitation power density at point z going in the direction of the incident light and in the opposite direction, respectively (it happened that in this chapter the z-axis is directed from top to bottom). Neglecting reflection at the inner interfaces of the heterostructure (it can be done if the difference between refractive indices of the layers is not too large, which is fulfilled for commonly used structures), we can calculate the magnitude of the excitation power density inside the structure just after the illuminated surface as

$$I^{(+)}_{z=0} = I_0 \, \frac{1 - R_0}{1 - R_0 R_N E^2} \qquad , \qquad E = \exp\left(-\int_0^L \alpha(z, \lambda_{exc}) dz\right) \tag{12.2}$$

where I_0 is the incident excitation power density, E is a factor describing decrease of the light intensity after crossing all the heterostructure, L is the heterostructure thickness, and $\alpha\,(z, \lambda_{exc})$ is the absorption coefficient at the excitation wavelength λ_{exc}. The factor $(1 - R_0 R_N E^2)^{-1}$ comes from the summation caused by the fact that light can pass through the structure several times as shown in Fig. 3 (let us also remind that $1+t+t^2+...+t^n+... = \frac{1}{1-t}$ for $0 < t < 1$).

Inside the structure, the excitation power density varies as

$$\begin{aligned} I^{(+)}(z) &= I^{(+)}_{z=0} \, \exp\left(-\int_0^z \alpha(z', \lambda_{exc}) dz'\right) \\ I^{(-)}_{z=L} &= I^{(+)}_{z=L} R_N \\ I^{(-)}(z) &= I^{(-)}_{z=L} \, \exp\left(-\int_z^L \alpha(z', \lambda_{exc}) dz'\right) \end{aligned} \tag{12.3}$$

The electron-hole pair generation rate is

$$G(z) = \left(I^{(+)}(z) + I^{(-)}(z)\right) \, \frac{\alpha(z, \lambda_{exc})}{q\,\hbar\omega_{exc}} \tag{12.4}$$

where $\hbar\omega_{exc}$ is the excitation photon energy.

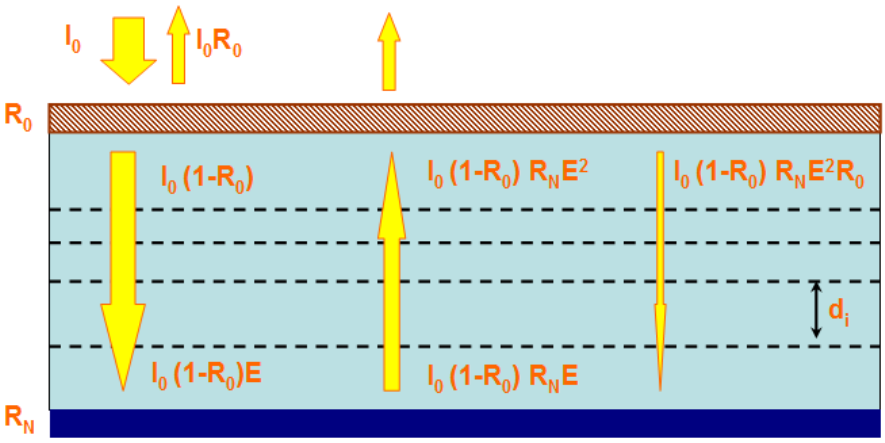

Figure 3: Light intensity in the structure with account of multiple reflections.

The fractions of the excitation power density which are reflected by the structure, transmitted through the structure, and absorbed inside the structure can be calculated as

$$\begin{aligned} R &= R_0 + \frac{I_{z=0}^{(+)}}{I_0}\,(1-R_0)\,R_N E^2 \\ T &= \frac{I_{z=0}^{(+)}}{I_0}\,(1-R_N)\,E \\ A &= 1-R-T = \frac{I_{z=0}^{(+)}}{I_0}\,(1-E)\,(1+R_N E) \end{aligned} \tag{12.5}$$

References

[1] J.F. Nye, "Physical Properties of crystals. Their representation by tensors and matrices", Oxford at the Clarendon Press (1957).

[2] A.E. Romanov, T.J. Baker, S. Nakamura, and J.S. Speck, "Strain-induced polarization in wurtzite III-nitride semipolar layers", J. Appl. Phys. 100, 023522 (2006).

[3] S.Yu. Karpov and Yu.N. Makarov, "Dislocation Effect on Light Emission Efficiency in Gallium Nitride", Appl. Phys. Lett. 81, 4721 (2002).

[4] W. Shockley and W.T. Read, Jr., "Statistics of the Recombinations of Holes and Electrons", Phys. Rev. 87, 835 (1952).

[5] M.A. Jacobson, D.K. Nelson, O.V. Konstantinov, and A.V. Matveentsev, "The tail of localized states at the forbidden band of quantum well in GaN and its effect on the photoluminescence spectrum at the laser excitation", Semiconductors 39, 1410 (2005).

[6] B.L. Gelmont and Z.N. Sokolova, "Auger recombination in direct-gap N-type semiconductors", Sov. Phys. Semicond. 16, 1067 (1982).

[7] K.A. Bulashevich and S.Yu. Karpov, "Is Auger recombination responsible for the efficiency rollover in III-nitride light-emitting diodes?", Phys. Stat. Solidi (c) 5, 2066 (2008).

[8] A.N. Pikhtin and A.D. Yas'kov, "Refraction of light in semiconductors (review)", Sov. Phys. Semicond. 22, 613 (1988).

[9] A.V. Ivanov, V.D. Kurnosov, K.V. Kurnosov, A.A. Marmalyuk, V.I. Romantsevich, Yu.L. Ryaboshtan, and R.V. Chernov, "Refractive indices of solid AlGaInAs solutions", Quantum Electronics 37, 545 (2007).

[10] "Quantum Well Lasers", Ed. P. Zory, Jr., Academic Press, San Diego (1993) Ch. 5.